MICROWAVE SCATTERING MODELS FOR CYLINDRICAL VEGETATION COMPONENTS

P. de Matthaeis and R. H. Lang

Department of Electrical and Computer Engineering
The George Washington University
Washington, DC 20052, USA

Abstract—This work is intended to investigate the accuracy of modelling simple cylindrical vegetation structures for microwave remote sensing applications. Plane wave scattering by dielectric cylinders of finite length and circular cross section is examined. Cylinders with a radius that varies linearly along the cylinder length — hereafter referred to as tapered cylinders — are also considered. Exact expressions for the scattering cross section do not exist for those objects. Numerical methods can provide accurate results, but they are computationally intensive and therefore less suitable when calculations on a large number of scatterers of different sizes and orientations are necessary. In this paper the scattering cross section of finite cylinders is computed by physical optics methods, which are faster and often employed in microwave vegetation models. Tapered cylinders are modelled by a number of coaxial finite cylinders stacked on top of each other. To check the validity of the results, the problems are also solved numerically by the moment method. For cases often encountered in vegetation studies, the results of the application of the approximate analytical methods are then compared with the corresponding numerical solution. For both constant-radius and tapered cylindrical structures, a good agreement with the numerical solution is found in the region of the main scattering lobe, which is the one of interest when considering complex media such as vegetation canopies. However, the accuracy of the approximate solutions decreases as the angle of the incident wave approaches the end-on angle.

1. INTRODUCTION

The problem of electromagnetic scattering by vegetation has received much attention in recent years, particularly with the deployment of air- and satellite-born Synthetic Aperture Radar (SAR) instruments. It is therefore especially important to have reliable models to characterize the electromagnetic behaviour of vegetation.

A vegetation canopy can be considered as a multilayered medium above a ground surface. Each layer can be modelled as an ensemble of individual dielectric objects of different type, size, and orientation [1]. Among the most common components in a vegetated medium are cylindrical structures, such as stems, branches or trunks, and needles [2, 3]. A taper, i.e., a linear variation of the radius along the cylinder length, can also be introduced to model trunks and branches more realistically [4]. The focus of the present work will be on those two types of dielectric objects.

The problem of electromagnetic scattering from such objects has been studied by several authors in the past with either analytical or numerical methods. Wait [5] was among the first ones to investigate and present an exact solution for scattering from an infinite circular cylinder at oblique incidence. Ruck *et al.* [6] also gave a summary of exact solutions for both conducting and homogeneous dielectric cylinders of infinite length.

An exact analytical solution for the scattering from finite-length cylinders does not exist, however a number of approximations have been studied. The Rayleigh-Gans approximation [7] is applicable

to tenuous scatterers for which the phase shift across the maximum dimension is small. Acquista [8] and Cohen *et al.* [9] extended the use of the Rayleigh-Gans approach to particles with low polarizability and slightly larger phase shift across them. Schiffer and Thielheim [10] introduced the an approximation for cylinders with one dimension electrically small and shorter than the other, i.e., either very thin or flat. Shepherd and Holt [11] applied the Fredholm integral equation method to the scattering of electromagnetic waves by finite cylinders of circular cross section, but their method also had limitations at the increase of the cylinder radius. Karam *et al.* [12, 13] used Schiffer and Thielheim's approximation to model dielectric discs and cylinders. Stiles and Sarabandi [14] provided a solution for thin dielectric cylinders with a broader range of validity, but still limited to small cross sections, and showed that Schiffer and Thielheim's approximation is a specific case of their solution.

The numerical treatment of the problem of scattering from a finite cylinder has generally been limited to the method of moments [15], while the finite elements method has been used mainly for problems involving inhomogeneous cylinders. Raz and Lewinsohn [16] investigated the volume and surface integral equation formulations relevant to the scattering and absorption of electromagnetic waves by thin, finite, and lossy dielectric cylinders. Papayiannakis *et al.* [17] treated the problem of scattering from a finite dielectric cylinder with dimensions comparable to the wavelength of the incident field, by solving an integral equation containing the free-space Green's function over the cylinder volume by the method of moments. Later, the same author [18] employed a transformation to reduce the three-dimensional integrals in the equation into two-dimensional ones. Finally, Mautz and Harrington [19] and Glisson and Wilton [22] introduced a simplification for axisymmetric scatterers — or bodies of revolutions — that reduces the problem to the solution of an integral equation along a curve by the method of moments.

In this paper, we will consider an approximate analytical model for finite dielectric cylinders developed by Seker and Schneider [20], and investigate its accuracy. Only prolate (i.e., with a length greater than the diameter) cylinders with circular cross section will be examined. The motivation of the present study is to show that for certain applications this analytical model can be used to estimate the scattering coefficient of cylinders that are not necessarily thin. In addition, we will study the scattering model for tapered cylinders introduced by [4], and show that in most cases it yields better results than the use of a single finite cylinder approximation.

Numerical methods are more accurate, but in random media

problems, such as vegetation with scatterers having many different orientations, it is only the main lobe of the bistatic scattering coefficient that is important. We will show that in many cases the analytical approximation is satisfactory enough to be used in place of the numerical methods, thus allowing a substantial reduction in computation time. In order to do this, after giving some definitions in the following Section 2, we will introduce a scattering model for finite dielectric cylinders. Such method is based on a physical optics approximation and will be explained in 3.1. The physical optics finite cylinder model will then be used in the tapered cylinder model described in 3.2. Section 4 will illustrate the body of revolution approach employed in combination with the method of moments to obtain a reference solution. The results of the application of the finite cylinder model and the tapered cylinder model will be presented in Section 5. Considerations about the computation time of the different methods will be made in 6, and finally the conclusions of this study will be given in Section 7.

2. DEFINITIONS

Consider a finitely-long circular dielectric cylinder of radius a and length L, with permittivity $\varepsilon = \varepsilon_0 \varepsilon_c$ and permeability $\mu = \mu_0$, located in free space. Here, ε_0 and μ_0 are the free space permittivity and permeability, respectively, and $\varepsilon_c = \varepsilon_r - j\varepsilon_j$ is the (complex) relative permittivity or dielectric constant of the cylinder. A Cartesian coordinate system (x, y, z) is defined with its origin in the center of the cylinder, and the z-axis coincident with the cylinder axis, as illustrated in Figure 1.

Assuming an angular frequency $\omega = 2\pi f$ (f being the frequency), and time dependence of the form $e^{j\omega t}$ for all electromagnetic quantities, the cylinder is considered being illuminated by a uniform plane wave

$$\boldsymbol{E}^{(i)}(\boldsymbol{r}) = \hat{\boldsymbol{q}}_i e^{-jk_0 \hat{\boldsymbol{k}}_i \cdot \boldsymbol{r}}, \qquad q = h, v. \tag{1}$$

In equation (1), $k_0 = \omega\sqrt{\mu_0 \varepsilon_0}$ is the free space wavenumber, and

$$\hat{\boldsymbol{k}}_i = -\sin\theta_i \cos\phi_i \hat{\boldsymbol{x}} - \sin\theta_i \sin\phi_i \hat{\boldsymbol{y}} - \cos\theta_i \hat{\boldsymbol{z}} \tag{2}$$

is the propagation vector of the incident wave from the direction (θ_i, ϕ_i). Here, unit vectors, such as $\hat{\boldsymbol{x}}$ or $\hat{\boldsymbol{k}}_i$, are denoted by bold faced symbols with hats on them.

A scattered wave is considered in the direction (θ_s, ϕ_s) with propagation vector

$$\hat{\boldsymbol{k}}_s = \sin\theta_s \cos\phi_s \hat{\boldsymbol{x}} + \sin\theta_s \sin\phi_s \hat{\boldsymbol{y}} + \cos\theta_s \hat{\boldsymbol{z}}. \tag{3}$$
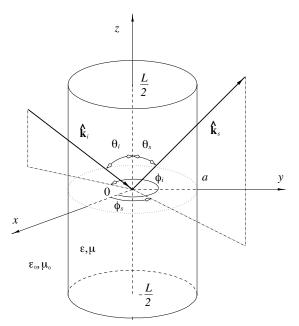
Figure 1. Geometry of the problem.

Horizontal and vertical polarizations of the incident and scattered waves are defined by the direction of their unit polarization vectors as follows:

$$\hat{\boldsymbol{h}}_i = \frac{\hat{\boldsymbol{k}}_i \times \hat{\boldsymbol{z}}}{|\hat{\boldsymbol{k}}_i \times \hat{\boldsymbol{z}}|}, \qquad \hat{\boldsymbol{v}}_i = \hat{\boldsymbol{h}}_i \times \hat{\boldsymbol{k}}_i \tag{4}$$

$$\hat{\boldsymbol{h}}_s = \frac{\hat{\boldsymbol{k}}_s \times \hat{\boldsymbol{z}}}{|\hat{\boldsymbol{k}}_s \times \hat{\boldsymbol{z}}|}, \qquad \hat{\boldsymbol{v}}_s = \hat{\boldsymbol{h}}_s \times \hat{\boldsymbol{k}}_s. \tag{5}$$

The scattered field in the radiation zone is given by:

$$\boldsymbol{E}^{(s)}(\boldsymbol{r}) \sim \boldsymbol{f}(\hat{\boldsymbol{k}}_s, \hat{\boldsymbol{k}}_i; \hat{\boldsymbol{q}}_i) \frac{e^{-jk_0 r}}{r} \tag{6}$$

where $\boldsymbol{f}(\hat{\boldsymbol{k}}_s, \hat{\boldsymbol{k}}_i; \hat{\boldsymbol{q}}_i)$ is the vector scattering amplitude of the object for incident polarization $\hat{\boldsymbol{q}}_i \in \{\hat{\boldsymbol{h}}_i, \hat{\boldsymbol{v}}_i\}$, and the observation point is $\boldsymbol{r} = r\hat{\boldsymbol{k}}_s$, r being the radial distance of the observer. Assuming a q-polarized incident wave as in (1), the bistatic scattering coefficient with scattered field having p-polarization is given by:

$$\sigma_{pq}(\theta_s, \phi_s; \theta_i, \phi_i) = 4\pi |f_{pq}(\hat{\boldsymbol{k}}_s, \hat{\boldsymbol{k}}_i)|^2, \quad p, q = h, v \tag{7}$$

where f_{pq} are the scalar scattering amplitudes in the p- and q-polarization (received and transmitted, respectively):

$$f_{pq}(\hat{\boldsymbol{k}}_s, \hat{\boldsymbol{k}}_i) = \hat{\boldsymbol{p}}_s \cdot \boldsymbol{f}(\hat{\boldsymbol{k}}_s, \hat{\boldsymbol{k}}_i; \hat{\boldsymbol{q}}_i), \quad p, q = h, v. \tag{8}$$

3. APPROXIMATE ANALYTICAL MODELS

3.1. Finite, Constant-Radius Cylinder Approximation

Consider the dielectric cylinder of radius a and length L defined in the previous section. The incident wave (1) induces an internal field $\boldsymbol{E}_{int}^q$ inside the cylinder. The scattering amplitude for the cylinder is related to the internal field by (see [10, 21] for details):

$$f_{pq}(\hat{\boldsymbol{k}}_s, \hat{\boldsymbol{k}}_i) = \frac{k_0^2(\varepsilon_c - 1)}{4\pi} \int_V \hat{\boldsymbol{p}}_s \cdot \boldsymbol{E}_{int}^q(\boldsymbol{r}') e^{jk_0\hat{\boldsymbol{k}}_s \cdot \boldsymbol{r}'} dV', \quad p, q = h, v \tag{9}$$

Because the internal fields within a finite-length cylinder are not known exactly, they are approximated by the internal fields inside an infinite cylinder of the same radius, orientation and dielectric constant. This assumption requires that the cylinder length be large compared to its radius, i.e.,

$$\frac{L}{a} \gg 1. \tag{10}$$

The internal electric field for horizontally (TE) or vertically (TM) polarized incident wave can be found in Wait [5]. The integration within the cylindrical volume V is carried out in [20], where the resulting expressions for the scattering amplitudes f_{hh}, f_{hv}, f_{vh} and f_{vv} are also given.

Such expressions are valid for cylinders of any thickness, as long as the constrain given in (10) is satisfied. However, if the cylinder is very thin, a further approximation can be applied. It is shown in [20] that if the radius a of the cylinder is small compared to its internal wavelength, a quasi-static approximation is utilized to reduce the complexity of the scattering amplitude expressions.

In this paper, the general case of a cylinder with an arbitrary radius a and length L satisfying (10) will be considered, and the expressions for f_{hh}, f_{hv}, f_{vh} and f_{vv} explicitly given in [20] will be used.

3.2. Tapered Cylinder Approximation

Consider a dielectric tapered cylinder of length L and radii a and b at the major and minor base, respectively, centered at the origin
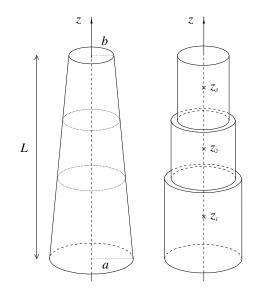
Figure 2. Tapered cylinder model.

of a Cartesian coordinate system, as shown in Figure 2. Let the permittivity and permeability of such body be $\varepsilon = \varepsilon_c \varepsilon_0$ and $\mu = \mu_0$, respectively, and the axis of the cylinder be coincident with the z-axis.

The simplest way to model such tapered cylinder is to approximate it with a finite cylinder of same length and volume. However, as it will also be shown later in this paper, this works well only when the taper is small. In general, it is more appropriate to divide the tapered cylinder into a number N_s of sections, and then approximate each one with a cylinder of like length and volume. This model has been introduced by [20], following measurements of trunk diameters at different heights. The approach is illustrated in Figure 2 for a number of sections $N_s = 3$. This approximation is valid when the taper is small:

$$R = \frac{a - b}{L} \gg 1. \tag{11}$$

In general, the higher the factor R, the larger the number of sections N_s needed to achieve a good approximation. The scattering amplitude of the m-th cylinder, translated by a distance z_m along the z-axis is:

$$\tilde{f}_{pq}^{(m)}(\hat{\boldsymbol{k}}_s, \hat{\boldsymbol{k}}_i) = f_{pq}^{(m)}(\hat{\boldsymbol{k}}_s, \hat{\boldsymbol{k}}_i)e^{-jk_0 z_m(\hat{\boldsymbol{k}}_i - \hat{\boldsymbol{k}}_s)\cdot\hat{\boldsymbol{z}}}, \ \ p,q = h,v, \ m = 1,\ldots,N_s \tag{12}$$

In (12), $f_{pq}^{(m)}(\hat{\boldsymbol{k}}_s, \hat{\boldsymbol{k}}_i)$ is the scattering amplitude of the cylinder centered at the origin, and the exponential term accounts for the phase shift in

both the incident and scattered wave produced by the translation of the cylinder by z_m.

Assuming no coupling exists between the cylinders, the total scattering amplitude of the configuration is the sum of N_s terms $\tilde{f}_{pq}^{(m)}(\hat{\boldsymbol{k}}_s, \hat{\boldsymbol{k}}_i)$ as in (12), i.e.,

$$f_{pq}(\hat{\boldsymbol{k}}_s, \hat{\boldsymbol{k}}_i) = \sum_{m=1}^{N_s} f_{pq}^{(m)}(\hat{\boldsymbol{k}}_s, \hat{\boldsymbol{k}}_i)e^{-jk_0 z_m(\hat{\boldsymbol{k}}_i - \hat{\boldsymbol{k}}_s)\cdot\hat{\boldsymbol{z}}}, \qquad p, q = h, v \quad (13)$$

The individual scattering amplitudes $f_{pq}^{(m)}(\hat{\boldsymbol{k}}_s, \hat{\boldsymbol{k}}_i)$ in (13) are determined using the finite cylinder approximation described in the previous section.

The rationale behind this approximation is the following. Consider a finite cylinder of length L, and divide it in N, sections of arbitrary length. The scattering amplitudes of all cylindrical sections are estimated using the finite cylinder model described in the previous Section 3.1, and added together according to (13), to yield the total scattering amplitude of the configuration. Since the contributions of the end currents from two contiguous cylindrical sections cancel with each other, the final result is no interaction between those sections. The only remaining effects in the sum (13) are those at the two terminal sections. The resulting scattering amplitude is therefore the same as that provided by the finite cylinder model for the original cylinder of length L.

The tapered cylinder model described in this section is a perturbation of the situation just illustrated. If the difference in radius between contiguous sections is small, only weak interactions exist between those adjoining cylinders, while the two terminal sections will experience the effect of replacing their internal fields with those of two infinite cylinders, as explained in the previous section.

4. NUMERICAL MODEL FOR BODY OF REVOLUTION

An exact solution is needed as a reference to evaluate the accuracy of the finite cylinder model and the tapered cylinder model introduced in the two previous sections. Since no closed-form exact analytical expressions are known for the scattering from finite or tapered cylinders, the only available option is to use a numerical analysis approach. Following the work of Glisson and Wilton [22], we have developed a method of moments code to determine the scattering from objects — such as the finite or the tapered cylinder — that can be modelled as bodies of revolution.

The result of the application of this numerical method is still an approximation to the exact solution. However, we have tested our algorithm on scatterers such as spheres, whose scattering coefficient theoretical expression is known analytically, and found that its results match the theory very well. In this paper we will consider the numerical solution as the reference to evaluate the accuracy of the finite cylinder and the tapered cylinder approximations.
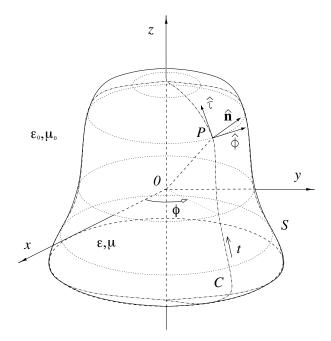

Figure 3. Body of revolution.

As shown in Figure 3, a body of revolution is obtained by rotation of a planar arc C — called the generating curve — about an axis, which is chosen as the z-axis of a Cartesian coordinate system. The surface S thus generated represents the boundary between free space and the material body, which is assumed as having permittivity $\varepsilon = \varepsilon_0 \varepsilon_c$ and permeability $\mu = \mu_0$. A point P on S is uniquely identified by a pair of variables (t, ϕ), where t is the curvilinear coordinate along the generating curve to which P belongs, and ϕ is the rotation or azimuth angle measured from the xz-plane. A right-handed triad $(\hat{\boldsymbol{n}}, \hat{\boldsymbol{\phi}}, \hat{\boldsymbol{\tau}})$ of orthonormal vectors is defined on S, with $\hat{\boldsymbol{n}}$ and $\hat{\boldsymbol{\tau}}$ being respectively the normal and the tangent unit vectors to S in the plane of the curve C. All these definitions are illustrated in Figure 3.

Let the body of revolution be illuminated by an incident plane

wave $\boldsymbol{E}^{(i)}$ with tangential component $\boldsymbol{E}_t^{(i)}$ on the surface S, that, in turn, induces an electric and magnetic field on S, $\boldsymbol{E}$ and $\boldsymbol{H}$. The equivalent tangential electric and magnetic currents $\boldsymbol{J}_t$, $\boldsymbol{M}_t$ on the surface S are defined as

$$\boldsymbol{J}_t(\boldsymbol{r}') = \boldsymbol{H}(\boldsymbol{r}) \times \hat{\boldsymbol{n}} \tag{14}$$
$$\boldsymbol{M}_t(\boldsymbol{r}') = \boldsymbol{E}(\boldsymbol{r}) \times \hat{\boldsymbol{n}} \tag{15}$$

It is important to understand that $\boldsymbol{J}_t$ and $\boldsymbol{M}_t$ are not real currents, but equivalent currents, in the sense that when considered in place of the induced internal currents they generate the same scattered field. They satisfy the following surface integral equations, on the exterior and interior surface, S^+ and S^-, respectively [23]:

$$\boldsymbol{M}_t(\boldsymbol{r}) \times \hat{\boldsymbol{n}} = 2\boldsymbol{E}_t^{(i)}(\boldsymbol{r}) - 2j\omega\mu_0(\underline{\boldsymbol{I}} - \hat{\boldsymbol{n}}\hat{\boldsymbol{n}})$$
$$\cdot \int_{S^+} \left[G(\boldsymbol{r},\boldsymbol{r}')\underline{\boldsymbol{I}} - \frac{\nabla G}{k^2}\nabla'_s \right] \cdot \boldsymbol{J}_t(\boldsymbol{r}')dS'$$
$$-2(\underline{\boldsymbol{I}} - \hat{\boldsymbol{n}}\hat{\boldsymbol{n}}) \int_{S^+} \nabla G(\boldsymbol{r},\boldsymbol{r}') \times \boldsymbol{M}_t(\boldsymbol{r}')dS', \quad \boldsymbol{r} \in S^+ \tag{16}$$

$$\boldsymbol{M}_t(\boldsymbol{r}) \times \hat{\boldsymbol{n}} = 2j\omega\mu_0(\underline{\boldsymbol{I}} - \hat{\boldsymbol{n}}\hat{\boldsymbol{n}}) \int_{S^-} \left[G(\boldsymbol{r},\boldsymbol{r}')\underline{\boldsymbol{I}} - \frac{\nabla G}{k^2}\nabla'_s \right] \cdot \boldsymbol{J}_t(\boldsymbol{r}')dS'$$
$$-2(\underline{\boldsymbol{I}} - \hat{\boldsymbol{n}}\hat{\boldsymbol{n}}) \int_{S^-} \nabla G(\boldsymbol{r},\boldsymbol{r}') \times \boldsymbol{M}_t(\boldsymbol{r}')dS', \quad \boldsymbol{r} \in S^- \tag{17}$$

where $\underline{\boldsymbol{I}}$ is the unit dyad,

$$\underline{\boldsymbol{I}} = \hat{\boldsymbol{x}}\hat{\boldsymbol{x}} + \hat{\boldsymbol{y}}\hat{\boldsymbol{y}} + \hat{\boldsymbol{z}}\hat{\boldsymbol{z}} = \hat{\boldsymbol{n}}\hat{\boldsymbol{n}} + \hat{\boldsymbol{\phi}}\hat{\boldsymbol{\phi}} + \hat{\boldsymbol{\tau}}\hat{\boldsymbol{\tau}} \tag{18}$$

k is the wavenumber,

$$k = \begin{cases} k_0 & \text{on } S^+ \\ k_0\sqrt{\varepsilon_c} & \text{on } S^- \end{cases} \tag{19}$$

$G(\boldsymbol{r},\boldsymbol{r}')$ is the scalar Green's function,

$$G(\boldsymbol{r},\boldsymbol{r}') = \frac{e^{-jk|\boldsymbol{r}-\boldsymbol{r}'|}}{4\pi|\boldsymbol{r}-\boldsymbol{r}'|} \tag{20}$$

and $\nabla'_s \cdot \boldsymbol{J}_t$ is the divergence of $\boldsymbol{J}_t$ on the surface S,

$$\nabla'_s \cdot \boldsymbol{J}_t(\boldsymbol{r}') = \hat{\boldsymbol{\tau}}' \frac{\partial \boldsymbol{J}_t}{\partial t'} + \hat{\boldsymbol{\phi}}' \frac{1}{\rho'} \frac{\partial \boldsymbol{J}_t}{\partial \phi'} \tag{21}$$

The exterior surface S^+ is defined as a surface infinitesimally close to the surface S and enclosing S itself. The interior surface S^- is defined

as a surface infinitesimally close to the surface S and enclosed by S itself.

The coupled surface integral equations are solved as follows. The rotational symmetry of the surface S is used to reduce the complexity of the problem. Using a Fourier series expansion in the azimuth angle ϕ of the incident electric field $\boldsymbol{E}_t^{(i)}$ and of the equivalent surface currents $\boldsymbol{J}_t$, $\boldsymbol{M}_t$, a pair of coupled integral equations for each Fourier mode is obtained. Each equation contains quantities that depend only on the curvilinear coordinate t. The dimensionality of the problem is thus reduced to one. The method of moments is then used to find the equivalent currents from these equations for each mode (see [15, 22]).

The coupled surface integral equations are solved with (1) as incident electric field in the polarization q. The equivalent surface currents $\boldsymbol{J}_t$, $\boldsymbol{M}_t$ that are found as solutions are subsequently used to compute the scattering amplitudes.

The vector scattering amplitude of the object in terms of the surface currents is:

$$
\boldsymbol{f}(\hat{\boldsymbol{k}}_s, \hat{\boldsymbol{k}}_i; \hat{\boldsymbol{q}}_i) = -\frac{1}{|\boldsymbol{E}_q^{(i)}|} \frac{jk_0}{r} \left[\sqrt{\frac{\varepsilon_0}{\mu_0}} \oint_S (\hat{\boldsymbol{\theta}}\hat{\boldsymbol{\theta}} + \hat{\boldsymbol{\phi}}\hat{\boldsymbol{\phi}}) \cdot \boldsymbol{J}_t(\boldsymbol{r}')e^{jk_0\hat{\boldsymbol{r}}\cdot\boldsymbol{r}'}dS' \right.
$$
$$
\left. + \oint_S (\hat{\boldsymbol{\phi}}\hat{\boldsymbol{\theta}} - \hat{\boldsymbol{\theta}}\hat{\boldsymbol{\phi}}) \cdot \boldsymbol{M}_t(\boldsymbol{r}')e^{jk_0\hat{\boldsymbol{r}}\cdot\boldsymbol{r}'}dS \right] \tag{22}
$$

where $(\hat{\boldsymbol{r}}, \hat{\boldsymbol{\theta}}, \hat{\boldsymbol{\phi}})$ is the triad of orthonormal vectors at the observation point, associated with a spherical coordinate system centered at the origin.

The p-component of the vector scattering amplitude (22) gives the scalar scattering amplitude $f_{pq}(\hat{\boldsymbol{k}}_s, \hat{\boldsymbol{k}}_i)$ in the   polarization produced by a q-polarized incident wave of the form (8). The bistatic scattering coefficient is then found from there through (7). In order to evaluate the integrals in (22), the equivalent surface currents $\boldsymbol{J}_t$, $\boldsymbol{M}_t$ are written as summations of Fourier modes and approximated in terms of basis functions used in the MOM solution of the integral equations (16), (17). As a result, the scattering amplitude will also have the form of a summation of an infinite number of modes, but the circulations are limited to a finite number of them, i.e., only to those modes that produce a significant contribution to the scattering.

5. APPLICATION TO SCATTERING FROM VEGETATION

In microwave remote sensing, a vegetation canopy is usually modelled as a layer of dielectric cylinders and disks placed over a half space

representing the ground. In the case of a forest such cylinders and disks represent trunks, branches, needles and leaves, while in the case of smaller vegetation such as agricultural crops, they represent stalks and leaves. The cylinders are circular, homogeneous, and lossy. Their dimensions and orientations are typical of trunks, branches, needles and stalks, and are based on ground data collected during experimental campaigns. Typical values for conifer forest are those given in [24] for hemlock trees in a boreal forest. Corn stalk parameters can be found in [25].

Table 1. Ground data.

vegetation type	vegetation element	radius a	length L
hemlock	secondary branch	1.8 mm	16 cm
hemlock	primary branch	0.6 cm	90 cm
hemlock	small trunk	3.0 cm	2.5 cm
hemlock	large trunk	10.0 cm	7.5 m
corn	stalk	1.25 cm	62.5 m

The relative dielectric constant ε_c of vegetation structures greatly depends on their water content. Tree trunk and branches are usually drier and therefore have a lower ε_c than corn stalks. For the sake of brevity, in the present paper we have opted to use only one value for the dielectric constant, but in our study we have also considered other values of ε_c, and found similar results. The value we have chosen is $\varepsilon_c = 18j6$, and is consistent with ground data measurements and Ulaby's empirical model [26].

In radar remote sensing, particularly when considering scattering from a layer of dielectric objects, the interest lies in the main scattering lobes. This is a consequence of the large number of scatterers in such vegetation media. Since the contributions from the single scatterers are added all together, the relative weigh of the scattering from the side lobes becomes negligible. Therefore, when comparing approximate and exact scattering coefficient in this paper, we consider acceptable an approximation that agrees with the theory inside the main scattering lobe and does not produce high scattering elsewhere. It has to be stressed that in cases where all scattering of any level must be taken into account — such as antenna applications — the conclusions of this article do no apply.

In the following two sections, we compare the values of the scattering coefficient estimated by the approximate methods with its exact values found numerically. This is done for both types of cylinders considered in this paper, in two separate sections. In particular, for various incident angles θ_i, ϕ_i, we determine the bistatic scattering coefficient over a range of scattering angles θ_s, ϕ_s using both methods. For the sake of brevity the illustration of results is limited to the case of scattering in the same plane $\phi = \phi_i$ of the incident wave, but we have found that similar conclusions apply for scattering at different azimuth angles ϕ_s.

To better quantify the accuracy of the analytical model, we introduce a parameter ϵ_{pp} to measure the error between exact and approximate solution over a range of scattering angles θ_s for a single incident angle θ_i. Let σ_{pp} and $\hat{\sigma}_{pp}$ be the values of the bistatic scattering coefficient obtained using the method of moments (i.e., the exact solution) and the analytical model (i.e., the approximate solution), for polarization $pp = hh, vv$, respectively. The absolute error in dB, ϵ_{pp}, of the finite cylinder model is defined as follows:

$$
\epsilon_{pp}(\theta_i) = \frac{1}{M_{pp}} \sum_{m=1}^{M_{pp}} \left| \hat{\sigma}_{pp}(\theta_s^{(m)}, \theta_i)[\text{dB}] - \sigma_{pp}(\theta_s^{(m)}, \theta_i)[\text{dB}] \right|, \ \ pp = hh, vv
$$

(23)

where the bistatic scattering coefficient is expressed in dB:

$$
\sigma_{pp}[\text{dB}] = 10 \log_{10}(\sigma_{pp}), \quad \hat{\sigma}_{pp}[\text{dB}] = 10 \log_{10}(\hat{\sigma}_{pp}), \quad pp = hh, vv
$$

(24)

The sum is carried out over a set of $m = 1, 2, \ldots, M_{pp}$ scattering angles $\theta_s^{(m)}$ where the scattering coefficient is no lower than $10\,\text{dB}$ below the peak value $\sigma_{pp}^{max}(\theta_i)$, i.e., such that

$$
\sigma_{pp}(\theta_s^{(m)}, \theta_i)[\text{dB}] \geq \sigma_{pp}^{max}(\theta_i)[\text{dB}] - 10\,\text{dB}, \quad pp = hh, vv
$$

(25)

The quantity ϵ_{pp} provides an estimate of the difference — expressed in dB — between the approximation and the exact solution over a range of angles where the level of scattering is high enough. In other words, ϵ_{pp} measures the area between the two exact and approximate dB curves σ_{pp} and $\hat{\sigma}_{pp}$ vs. θ_i, limited to the values $\theta_s^{(m)}$ of the scattering angle for which σ_{pp} satisfies expression (25). The error could be defined in many other different ways. Here we choose the definition (23) because of its simplicity and intuitive meaning, and we will use it merely as a tool to compare how the accuracy changes with the incident angles and the cylinder size.

5.1. Finite, Constant-Radius Cylinder

In order to investigate the accuracy of the finite cylinder model, in this section we consider a number of cases of cylinders with different dimensions, chosen consistently with the ground data in [24] and [25].

Since the finite cylinder model assumes that the currents inside the cylinder are the same as if the cylinder were infinite, one would expect that the accuracy of the approximation decreases for shorter cylinders with a smaller length-to-radius ratio. However, we will see that for incident waves sufficiently close to the normal to the cylinder axis, the error is still small even in such cases.

The general shape of the scattering pattern of a dielectric cylinder is illustrated in Figure 4. The amplitude of the scattering has its maximum in a conical region also referred to as the scattering cone. In a section $\phi = \phi_i$ of the scattering pattern there will be two relative maxima corresponding to the main scattering cone, one in the forward direction, the other one in the specular direction with respect to the cylinder side.
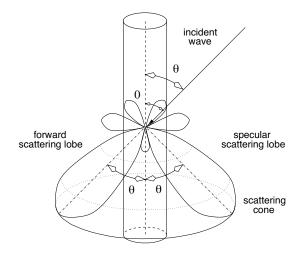

Figure 4. Scattering pattern of a cylinder.

In the following, the normalized bistatic scattering coefficient $\sigma/(\pi a^2)$ will be plotted as a function of the scattering angle for a fixed incident angle, in both hh- and vv-polarization. The scattering angle θ_s in the plots ranges between $0°$ and $180°$, therefore only the specular lobe at $\theta_s = 180° - \theta_i$ will be visible.

The first case examined is a cylinder of length $L = 10.0\lambda$ and radius $a = 0.04\lambda$. For a wavelength $\lambda = 60\,\text{cm}$ (or $f = 500\,\text{MHz}$, in P-band), this corresponds to a tree trunk $6\,\text{m}$ long with a diameter of
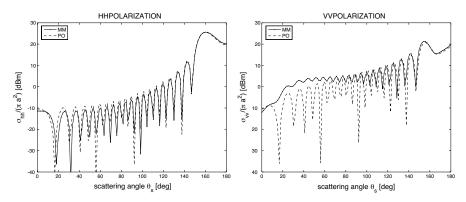
Figure 5. Normalized bistatic scattering coefficient vs. scattering angle for finite dielectric cylinder with $L = 10.0\lambda$, $a = 0.04\lambda$, and incident angle $\theta_i = 20°$.

4.8 cm. This cylinder is several wavelengths long and its length and radius satisfy the condition (10). The normalized bistatic scattering coefficient $\sigma/(\pi a^2)$ is plotted in Figure 5 as a function of the scattering angle θ_s for an incident angle $\theta_i = 20°$, in both hh- and vv-polarization. The solid curve represents the method of moments numerical solution (MM), while the dashed curve is obtained using the approximate physical optics analytical solution (PO). There is very good agreement between the two solutions except for vv-polarization at angles θ_s far from the specular scattering lobe located at approximately $\theta_s = 160°$.

As the cylinder becomes thicker, i.e., the ratio L/a decreases, one would expect the finite cylinder model to lose its accuracy. Nevertheless, we will see that in such case the approximation is still satisfactory for incident angles θ_i close to the normal to the cylinder axis. There is a possible intuitive explanation for this behaviour. In the analytical model, the finite cylinder is treated as infinite and the effects of its ends are not accounted for. The contribution of such end-on scattering becomes more pronounced in thicker cylinders due to the larger area of the ends. However, the ends are almost invisible to normal or quasi-normal incident waves, and therefore in that case their contribution to the scattering is negligible.

Figure 6 shows the normalized bistatic scattering coefficient vs. the scattering angle for a cylinder with the same length and permittivity as in Figure 5, but with a radius $a = 0.4\lambda$, for an incident angle $\theta_i = 20°$. Although it is still $L \gg a$, the plots of the exact and approximate now differ, especially for vv-polarization, even in the main lobe. The actual amplitude of the scattering off the main scattering cone is much
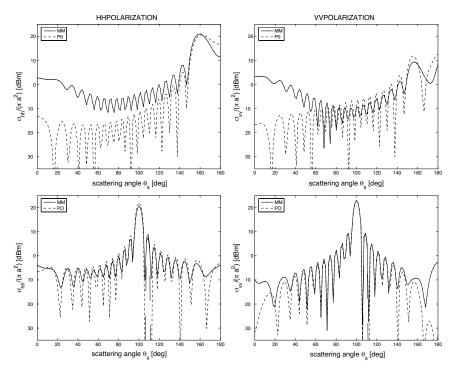
Figure 6. Normalized bistatic scattering coefficient vs. scattering angle for finite dielectric cylinder with $L = 10.0\lambda$, $a = 0.4\lambda$, $\varepsilon_r = 18j6$, and incident angle $\theta_i = 20°$ (top) and $\theta_i = 80°$ (bottom).

higher than what predicted by the analytical model. It is reasonable to conclude that the main contribution to the scattering at those angles θ_s comes from the ends, while in the main lobe it comes from the sides. Nonetheless, as it has been discussed earlier, the agreement improves considerably when the incident angle approaches the normal to the cylinder axis. Indeed, for a higher incident angle such as $\theta_i = 80°$, shown in the two plots at the bottom of Figure 6, the agreement is very good, except for a couple of dB difference at the peak value of the hh-polarization. In this case, the ends are almost invisible when looking at the cylinder from the angle θ_i, which could explain why the analytical model yields accurate results.

As explained previously, when treating remote sensing problems, only the scattering within 10 dB of the peak value is relevant, therefore we are concerned with achieving a good approximation only in the region surrounding the maxima. This means that for the thinner cylinder illustrated in Figure 5, there is very good agreement, while for

the thicker cylinder in Figure 6, there are some problems at $\theta_i = 20°$ due to the scattering from the ends that are not accounted for in the approximate model. Such problems are more pronounced for vv-polarization, a possible explanation for which being the discontinuity in the perpendicular component at the cylinder ends, but disappear at $\theta_i = 80°$.

To better understand how the accuracy changes with the cylinder dimensions as well as with the incident angle, we now compute the absolute error defined by (23). We consider two different values for the radius: $a = 0.04\lambda$ to represent a thin cylinder, and $a = 0.4\lambda$ to represent a thick cylinder. In both cases, the absolute errors ϵ_{hh} and ϵ_{vv} are plotted versus the incident angle θ_i for three different values of the length, e.g., long, medium, and short.
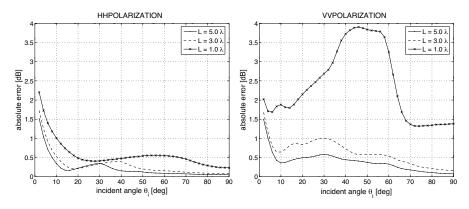

Figure 7. Absolute error vs. incident angle for finite dielectric cylinder with $a = 0.04\lambda$, $\varepsilon_r = 18j6$, $L = 5.0\lambda$, 3.0λ, and 1.0λ, for hh- and vv-polarization.

The thin cylinder cases ($a = 0.04\lambda$) are shown in Figure 7. The cylinder lengths are $L = \lambda$, 3λ, and 5λ, with the hh- and vv-polarization on the left and right, respectively. All these cylinders have $a \ll L$, in particular $L/a = 25$, 75, and 625, respectively. If we consider an absolute error below 2 dB as acceptable, then the agreement between finite cylinder model and numerical solution at hh-polarization is excellent at most angles and for most lengths. The only exception is the shortest cylinder ($L = \lambda$), perhaps due to resonances. As expected, the error is lower for longer cylinders because the infinite cylinder assumption is more correct, and decreases as the incident angle increases since the end-on effect becomes less important. Also to be noted is the fact that ϵ_{vv} is generally higher than the corresponding ϵ_{hh}.
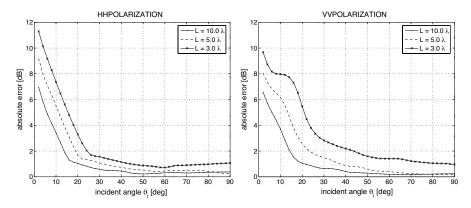
Figure 8. Absolute error vs. incident angle for finite dielectric cylinder with $a = 0.4\lambda$, $\varepsilon_r = 18j6$, $L = 10.0\lambda$, 5.0λ, and 3.0λ, for hh- and vv-polarization.

Figure 8 illustrates three thicker cylinder cases, with a radius $a = 0.4\lambda$ and lengths $L = \lambda, 5\lambda$, and 10λ, i.e., $L/a = 7.5$, 12.5, and 25, respectively. The most obvious comment is that the error in both polarizations is much higher than for the previous cases of Figure 6, which is expected given the lower value of L/a. There seems to be a threshold scattering angle θ_i^o below which the error increases as θ_i decreases, and above which the error remains fairly constant. Supposedly, those two regions — i.e, $\theta_i < \theta_i^o$ and $\theta_i > \theta_i^o$ — correspond to situations where end-on effects respectively have or don't have a significant effect on the main scattering cone. Such threshold value of θ_i decreases with the cylinder length, and varies between $15°$ for the longest cylinder, and $25°$ for the shortest. The approximation can be considered good (i.e., with an error lower than $2\,\text{dB}$) for angles that vary between $\theta_i > \theta_i^o = 15°$ for the longest cylinder, and $\theta_i > \theta_i^o = 40°$ for the shortest cylinder at vv-polarization. As also seen in the case of Figure 6, the analytical model performance is slightly worse at vv-polarization than at hh-polarization, especially for shorter cylinders.

5.2. Tapered Cylinder

Two cylinders of length $L = 10.0\lambda$ and different taper have been considered to illustrate the accuracy of the tapered cylinder model described in Section 3.2. For each case, the results of the numerical code are plotted together with the approximate solutions obtained using only one cylinder (cfr. equation (9)) and the tapered cylinder model (cfr. equation (13)) with two and four cylinders. The parameters

a, b and L are defined in Figure 2, and a_m is the radius of the cylinder replacing the m-th section ($m = 1, 2, \ldots, N_s$). A summary of the values of the cylinder lengths and radii used in the approximations is given in Table 2. A relative dielectric constant $\varepsilon_c = 18 - j6$ is assumed, i.e., the same value used in the previous section for the analysis of the finite cylinder model.

Table 2. Geometric parameters used in tapered cylinder approximations.

	$a = 0.7\lambda$, $b = 0.1\lambda$			$a = 0.5\lambda$, $b = 0.3\lambda$		
No. of cylinders N_s	1	2	4	1	2	4
$(L/N_s)/\lambda$	10.0	5.0	2.5	10.0	5.0	2.5
a_1/λ	0.4	0.55	0.625	0.4	0.45	0.475
a_2/λ		0.25	0.475		0.35	0.425
a_3/λ			0.325			0.375
a_4/λ			0.175			0.325

Figure 9 shows the normalized bistatic scattering coefficient vs. scattering angle for a tapered dielectric cylinder with $L = 10.0\lambda$, $a = 0.7\lambda$, $b = 0.1\lambda$, for a wave incident at an angle $\theta_i = 40°$. This cylinder has a taper factor — as defined in (11) — $R = 0.06$. In these plots, we have chosen a range of scattering angles $120° \leq \theta_s \leq 240°$ in order to show both the specular and the forward scattering lobe.

Note how the approximation with a single cylinder is inadequate, particularly around the specular scattering lobe, which is not located at the correct angle θ_s. Such displacement occurs because the slope of the side walls of the tapered cylinder cannot be modelled using only one cylinder. The direction of the forward scattering lobe, on the other hand, is not affected by the taper, and is correctly estimated by the approximate model. The use of two stacked cylinders (of length and radii given in Table 2) leads to a significant improvement. The main scattering lobe is now closer to its correct location, but there is still the problem of a high side lobe around $\theta_s = 150°$. The approximation with four cylinders brings the main lobe even closer to its correct position and — more important — lowers the sidelobes. Employing more than four cylinders still increases the accuracy, but the improvement is quite small.

Figure 10 illustrates the case of a tapered cylinder of the same length and volume as the cylinder in Figure 9, but with less taper,
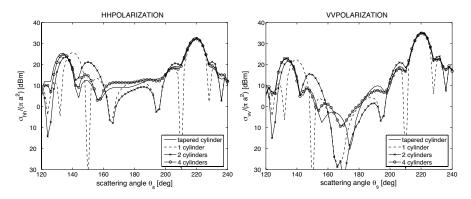
Figure 9. Normalized bistatic scattering coefficient vs. scattering angle for tapered dielectric cylinder with $L = 10.0\lambda$, $a = 0.7\lambda$, $b = 0.1\lambda$, and incident angle $\theta_i = 40°$. hh- and vv-polarization (left and right, respectively).
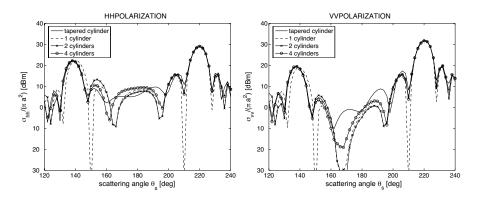

Figure 10. Normalized bistatic scattering coefficient vs. scattering angle for tapered dielectric cylinder with $L = 10.0\lambda$, $a = 0.5\lambda$, $b = 0.3\lambda$, and incident angle $\theta_i = 40°$. hh- and vv-polarization (left and right, respectively).

specifically with $a = 0.5\lambda$, $b = 0.3\lambda$, which results in a taper factor $R = 0.02$. The wave is incident from an angle $\theta_i = 40°$ as in the previous case. As one would expect given the smaller taper, the tapered cylinder model works much better in this situation, and even the one cylinder approximation exhibits only a small displacement in the main scattering lobe. In both Figures 9 and 10, it is evident that the analytical approximation works better in the forward scattering direction. This behaviour is probably due to the fact that the forward

scattering depends more on the dielectric properties of the cylinder, which are not approximated, while the scattering in the specular direction is more affected by the geometry, which depends on the model used. The error plots in Figure 11 help understand how the accuracy of the various approximations changes with the incident angle θ_i. The definition of the errors ϵ_{hh} and ϵ_{vv} is still the same as in (23).
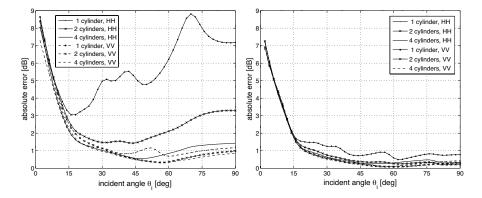

Figure 11. Error vs. incident angle for tapered dielectric cylinder with $L = 10.0\lambda$, (left) $a = 0.7\lambda$, $a_2 = 0.1\lambda$, and (right) $a = 0.5\lambda$, $b = 0.3\lambda$. Solid lines are hh-pol, dashed lines vv-pol.

The first of them is the long tapered cylinder of Figure 9, with $L = 10.0\lambda$, $a = 0.7\lambda$, $a_2 = 0.1\lambda$, and $R = 0.06$. Its absolute dB error is plotted at the left of Figure 11 as a function of the incident angle θ_i. As already noted in Figure 9, the single cylinder solution does not provide a good approximation for the tapered cylinder around the specular scattering lobe. The curves on the left of Figure 11 confirm that by showing an error between 3 dB and 10 dB at most incident angles in hh-polarization. Such a large error is mostly caused by the misplacement of the specular scattering lobe by the analytical approximation. For the same reason, using two cylinders produces a lower — but still unacceptable — error at hh-polarization. The approximation with four stacked cylinders yields the best results, the error being below 1.5 dB at the most angles, except for low incident angles, i.e., $\theta_i < 15°$. The problem of misplacement of the specular lobe in the approximation does not seem to affect the vv-polarization. In reality, as obvious from Figure 9, the problem is present at both polarizations, but since at vv-polarization the specular scattering lobe is more than 10 dB lower than the forward scattering lobe, it does not enter in the calculation of the error as defined in (23).

On the right side of Figure 11 are the error plots for the cylinder

of Figure 10, with $L = 10.0\lambda$, and $a = 0.5\lambda$, $b = 0.3\lambda$, and $R = 0.02$. The cylinder has a smaller taper, and a good approximation is already achieved with a finite cylinder of the same length and volume, with no major improvement using the tapered cylinder approximation. On the other hand, comparison between the two plots in Figure 11 indicates that the error at low incident angles is not affected by the taper. The most obvious conclusion is that the end-on effect are predominant there and cannot be predicted accurately by any of the approximate models here used.

6. COMPARISON OF COMPUTATIONAL TIMES

In this section we will make a comparison of the computational times of the various methods, in order to show the advantage of choosing the analytical approximations over the numerical solution approach. In order to estimate and compare computation times of the different methods, we make the following considerations.

The number of calculations needed to evaluate the scattering coefficient using the finite cylinder model does not depend on the cylinder length and is constant for a fixed vale of its radius. This happens because the expression used to compute the scattering amplitudes is a series summation with a number of terms that increases with the radius of the cylinder. In practice this number has been chosen large enough to achieve convergence in all cases considered in this comparison. Under this assumption, let T_{FC} be defined as the computation time of the scattering coefficient by the finite cylinder model.

The tapered cylinder model requires — as a first step — the calculation of the scattering amplitudes of the N_s individual cylinders that approximate sections of the original tapered cylinder. The scattering amplitudes are then used in expression (13) to yield the scattering amplitude of the entire tapered cylinder. Therefore, if one neglects the time need to perform such summation, the computation time of the tapered cylinder model will be

$$T_{TC} = N_s T_{FC}, \tag{26}$$

which depends on the number N_s of sections in the approximation, but not directly on the tapered cylinder length.

On the other hand, the method of moments involves the selection of a set of N points on the generating curve C and requires a number of calculation that increases as N^2. The number of points N varies in proportion to the length l of the generating curve C in the representation of the cylinder as a body of revolution, measured in

wavelengths λ. For a finite cylinder of length L and radius a, the length l of the generating curve C is $l = L+2a$, while $l = L+a+b$ for a tapered cylinder of length L and radii a, b. Therefore, it is reasonable to expect the computation time T_{MM} of the method of moment algorithm to increase approximately with the square of the cylinder length.

Empirically, we found the following approximate relationship between T_{MM} and T_{FC}:

$$T_{MM} = 3M \left(\frac{l}{\lambda}\right)^2 T_{FC} = 3M \left(\frac{L+2a}{\lambda}\right)^2 T_{FC}. \qquad (27)$$

where M is the number of modes used in the numerical algorithm.

Similarly, if the method of moments is used to find the scattering coefficient of a tapered cylinder, we found, using (26) to (28):

$$T_{MM} = 3M \left(\frac{l}{\lambda}\right)^2 T_{FC} = 3\frac{M}{N_s} \left(\frac{L+2a+b}{\lambda}\right)^2 T_{TC}. \qquad (28)$$

In order to examine the gain in computational speed, T_{TC} and T_{MM} have been estimated using expressions (26) and (28) for four tapered cylinders with $a = 0.6\lambda$, $b = 0.2\lambda$, and lengths $L = \lambda$, $L = 3\lambda$, $L = 5\lambda$, and $L = 10\lambda$. As an example, we consider a computer system on which the finite cylinder program needs a time $T_{FC} = 5\,\text{sec}$ to calculate the scattering coefficients. For all four cases, the number of sections in the tapered cylinder approximations is chosen as $N_s = 4$, therefore according to (26) the computation time is $T_{TC} = 20\,\text{sec}$.

The computational time T_{MM} if the numerical algorithm has been estimated through expression (28), and listed in Table 3, where the ratio T_{MM}/T_{TC} is also given. A number of modes $M = 5$ has been found to achieve good accuracy in the numerical solution in these particular cases, and used in (28).

Table 3. Comparison of computation time between analytical model and numerical algorithm for four tapered cylinders of length L and $a = 0.6\lambda$, $b = 0.2\lambda$.

length L	T_{MM}	T_{MM}/T_{TC}
λ	4 min	12
3λ	18 min	54
5λ	42 min	126
10λ	145 min	438

The values in Table 3 clearly show the great gain in computational efficiency at the cost of some loss of accuracy. Indeed, it is easy to see that even for a rather short cylinder of length $L = 3\lambda$, a computation time of $T_{MM} = 18\,\text{min}$ for the numerical approach compared to $T_{TC} = 20\,\text{sec}$ for the analytical approximation makes the latter preferable when dealing with a media where thousands cylinders of different sizes are present and estimation of the scattering coefficient from each cylinder is needed.

7. CONCLUSIONS

In this paper, we have considered analytical approximations for two different types of finite cylinders, and evaluated their accuracy. We have showed that for cylinder sizes and dielectric constant similar to those used to represent vegetation elements, such approximations work well in the main lobes This is indeed what we are most concerned with when studying remote sensing from vegetation.

While the physical optics solution for the finite cylinder works very well and is readily and safely usable in vegetation models, the tapered cylinder approximation requires more attention in the choice of the number N_s of cylinders, in order to reduce the error due to the displacement of the specular scattering lobe. The results also prove that when the taper is significant, the single cylinder approximation is not adequate for a tapered cylinder.

As seen in the previous section, the relative small loss in accuracy suffered by the use of such models is outbalanced by a tremendous gain in computational speed. However, more work could be done to try to model the end-on scattering. The integration of such a model into the approximations examined in this paper could allow their use in a broader range of electromagnetic problems.

REFERENCES

1. Fung, A. K., *Microwave Scattering and Emission Models and Their Applications*, 1994.
2. Ulaby, F. T., K. Sarabandi, K. McDonald, and M. C. Dobson, "Michigan microwave canopy scattering model," *International Journal of Remote Sensing*, Vol. 11, 1223–1253, 1990.
3. Karam, M. A., A. K. Fung, R. H. Lang, and N. S. Chauhan, "A microwave scattering model for layered vegetation," *IEEE Transactions on Geoscience and Remote Sensing*, Vol. 30, 767–784, 1992.

4. Lang, R. H., S. C. Chauhan, K. J. Ranson, and O. Kilik, "Modeling P-band SAR returns from a red pine stand," *Remote Sensing of the Environment*, Vol. 47, 132–141, 1994.

5. Wait, J. R., "Scattering of a plane wave from a right circular dielectric cylinder at oblique incidence," *Canadian Journal of Physics*, Vol. 33, 189–195, 1955.

6. Ruck, G. T., D. E. Barrick, W. D. Stuart, and C. K. Krichbaum, *Radar Cross Section Handbook*, 1970.

7. Gans, R., *Annalen der Physik*, Vol. 76, 1925.

8. Acquista, C., "Light scattering by tenuous particles: a generalization of the Rayleigh-Gans-Rocard approach," *Applied Optics*, Vol. 15, 2932–2936, 1976.

9. Cohen, L. D., R. D. Haracz, A. Cohen, and C. Acquista, "Scattering of light from arbitrarily oriented finite cylinders," *Applied Optics*, Vol. 22, 742–748, 1983.

10. Schiffer, R. and O. Thielheim, "Light scattering by dielectric needles and disks," *Journal of Applied Physics*, Vol. 50, 2476–2483, 1979.

11. Shepherd, J. W. and A. R. Holt, "The scattering of electromagnetic radiation from finite dielectric circular cylinders," *J. Phys. A: Math. Gen.*, Vol. 16, 651–662, 1983.

12. Karam, M. A. and A. K. Fung, "Electromagnetic scattering from a layer of finite-length, randomly oriented dielectric circular cylinders over a rough interface with application to vegetation," *International Journal of Remote Sensing*, Vol. 9, 1109–1134, 1988.

13. Karam, M. A., A. K. Fung, and Y. M. M. Antar, "Electromagnetic wave scattering from some vegetation samples," *IEEE Transactions on Geoscience and Remote Sensing*, Vol. 26, 799–808, 1988.

14. Stiles, J. M. and K. Sarabandi, "A scattering model for thin dielectric cylinders of arbitrary cross section and electrical length," *IEEE Transactions on Antennas and Propagation*, Vol. 44, 260–266, 1996.

15. Harrington, R. F., *Field Computations by Moment Methods*, 1968.

16. Raz, S. and J. A. Lewinsohn, "Scattering and absorption by a thin, finite dielectric cylinder," *Applied Physics*, Vol. 22, 61–69, 1980.

17. Papagiannakis, A. G. and E. E. Keiezis, "Scattering from a dielectric cylinder of finite length," *IEEE Transactions on Antennas and Propagation*, Vol. 31, 725–731, 1983.

18. Papagiannakis, A. G., "Application of a point-matching MoM reduced scheme to scattering from finite cylinders," *IEEE*

Transactions on Microwave Theory and Techniques, Vol. 45, 1545–1553, 1997.

19. Mautz, J. R. and R. F. Harrington, "Electromagnetic scattering from a homogeneous material body of revolution," *Archiv für Elektronik und Ubertragungstechnik*, Vol. 33, 71–80, 1979.

20. Seiker, S. S. and A. Schneider, "Electromagnetic scattering from a dielectric cylinder of finite length," *IEEE Transactions on Antennas and Propagation*, Vol. 36, 303–307, 1998.

21. Le Vine, D. M., R. Meneghini, R. H. Lang, and S. S. Seker, "Scattering model from arbitrary oriented dielectric discs in the physical optics regime," *Journal of the Optical Society of America*, Vol. 73, 1255–1262, 1994.

22. Glisson, A. K. and D. R. Wilton, "Simple and efficient numerical methods for problems of electromagnetic radiation and scattering from surfaces," *IEEE Transactions on Antennas and Propagation*, Vol. 28, 593–603, 1980.

23. Poggio, A. J. and E. K. Miller, "Integral equation solutions of three-dimensional scattering problems," *Computer Techniaues for Electromagnetics*, Chapter 4, 1973.

24. Chauhan, S. C., R. H. Lang, and K. J. Ranson, "Radar modeling of a boreal forest," *IEEE Transactions on Geoscience and Remote Sensing*, Vol. 29, 627–638, 1991.

25. Chauhan, S. C., D. M. Le Vine, and R. H. Lang, "Discrete scatter model for microwave radar and radiometer response to corn: comparison of theory and data," *IEEE Transactions on Geoscience and Remote Sensing*, Vol. 32, 416–426, 1994.

26. Ulaby, F. T. and M. A. El-Rayes, "Microwave dielectric spectrum of vegetation — Part II: Dual dispersion model," *IEEE Transactions on Geoscience and Remote Sensing*, Vol. 25, 550–557, 1987.

Paolo de Matthaeis was born in Rome, Italy, in 1966. He received the Laurea degree (Summa cum Laude) in Electronic Engineering from the University of Rome "Tor Vergata", Italy, in 1991. In 1993–1994 he was with the European Space Agency at ESTEC in The Netherlands under the Young Graduate l ainee program. Afterwards, he worked on the analysis of SIR-C/X-SAR data at the Remote Sensing Laboratory at the University of Rome "Tor Vergata" with a grant from the Italian Space Agency (ASI). He is currently completing a Ph.D. degree in Electrical and Computer Engineering at The George Washington University in Washington, DC. He is a member of the IEEE, and his research interests include electromagnetics and radar remote sensing.

Roger H. Lang has received the B.S. and M.S. degrees in electrical engineering in 1962 and 1964, respectively, and Ph.D. degree in electrophysics in 1968, all from the Polytechnic University, New York City, New York. He has worked at Bell Telephone Laboratories on satellite antennas during 1963–1964, and has done postdoctoral work on wave propagation in random media at the Courant Institute of Mathematical Science of New York University during 1968–1970 before joining the George Washington University, Washington, DC. He now holds the position of Professor in the Department of Electrical and Computer Engineering at The George Washington University. He has been elected a Fellow of the IEEE in 1989 where he has been cited for his work in modeling microwave of propagation and scattering in vegetation. He is presently Secretary of USNC/URSI Commission F, a member of the Editorial Board of Waves in Random and Complex Media.